CHEMISTRY OF MATERIALS

pubs.acs.org/cm

Article

Divalent Chromophores in Trigonal Bipyramidal Coordination: $YIn_{1-x}(M^{2+}_{0.5}Ti_{0.5})_xO_3$ (M = Co, Mn, Ni, Fe) Solid Solutions

Published as part of Chemistry of Materials special issue "Celebrating Myung-Hwan Whangbo on the Occasion of his 80th Birthday".

Anjali Verma, Jun Li, Chung Yi Hsu, Arthur P. Ramirez, Fanny Rodolakis, Daniel Haskel, and M. A. Subramanian*

Cite This: https://doi.org/10.1021/acs.chemmater.6c01433

Read Online

ACCESS | Metrics & More | Article Recommendations | Supporting Information

ABSTRACT: The rational design of inorganic pigments with predetermined colors remains challenging due to the complex interplay of factors governing their optical properties, among which the oxidation state of the chromophore plays a critical role. Chromophores obeying selection rules are preferred for producing intense colors in transition-metal oxides. The intense blue color in the hexagonal $YIn_{1-x}Mn_xO_3$ (YInMn blue) system originates from the allowed d−d transition of Mn^{3+} in trigonal bipyramidal (TBP) coordination. Motivated by this, a series of hexagonal $YIn_{1-x}(M^{2+}_{0.5}Ti_{0.5})_xO_3$ (M = Co, Co/Zn, Mn, Ni, Fe) solid solutions were synthesized in evacuated quartz tubes to stabilize divalent chromophores. The Co and Co/Zn containing series exhibit intense, tunable magenta colors, the Mn-containing series shows olive green hues, the Ni-containing series displays lime green colors, and the Fe-containing series produces tunable brown shades. Neutron diffraction refinements confirmed the proposed crystal structures and compositions, while optical, magnetic, and X-ray absorption spectroscopy (XAS) verified the divalent oxidation state of the chromophore ions in the as-synthesized samples. Upon reheating in air, all compositions except the Ni-containing series exhibited a noticeable color change, which was largely reversible upon subsequent reduction, with colors returning to shades similar to the original samples. Combined optical, magnetic, and XAS analyses indicate oxidation of Co, Mn, and Fe from M^{2+} toward M^{3+}, whereas optical and magnetic measurements suggest that Ni remains in the +2 oxidation state.

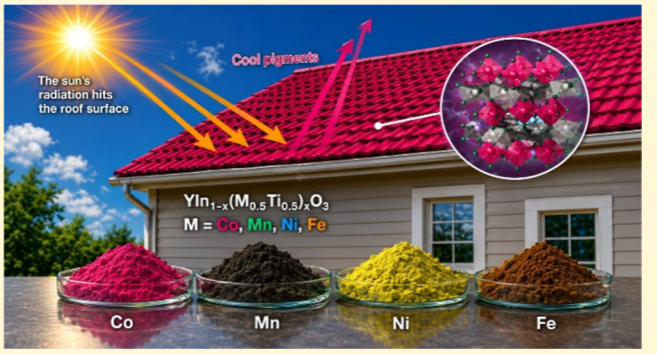

INTRODUCTION

Materials with various colors have always fascinated people from prehistory to the present. They bring joy to our daily lives by making the world a more beautiful place to live in and by influencing our feelings. The search for materials with intense and durable colors has occupied mankind since prehistory. Inorganic pigments are particularly interesting colored solids finding multifunctional applications, especially as artist colors, exterior coatings, and also as cool heat-reflecting paints.[1−6] Generally, inorganic pigments are either oxides, sulfides, sulfoselenides, or oxyhalides.[7] Among the various inorganic pigments, transition metal containing oxides form a series of compounds with a uniquely wide range of optical properties.[8] Transition metal cations engender color because they have electronic transition energies that resonate with frequencies in the visible range. Among the various electronic transitions, the d−d transition is the most common origin of color in transition metal compounds and minerals. The origin and intensity of these electronic transitions can be further understood in terms of orbital interactions, symmetry, and energy-level considerations within the molecular orbital framework.[9−12]

To design intense inorganic pigments with targeted colors, it is essential to understand the multiple factors influencing their optical properties. The current approaches to predicting color in new materials go beyond the traditional attribution of specific hues to particular elements in a solid, such as associating greenish blue with copper, deep blue with cobalt, red with lead or cadmium, or green with chromium or nickel, which can often be inaccurate.[11] Two important factors influencing the color are the coordination environment and the

Received: May 19, 2026
Revised: July 11, 2026
Accepted: July 14, 2026
Published: July 22, 2026

oxidation state of the chromophore.[11,13] To create intense pigments, the chromophore responsible for color through d−d transitions must obey the Laporte and spin selection rules.[14] Consequently, chromophores occupying noncentrosymmetric coordination sites, such as tetrahedral or trigonal bipyramidal (TBP) geometries, are particularly favorable for achieving intense color, as relaxation of the Laporte selection rule occurs through d−p mixing.

While exploring a new class of manganese-containing oxides for applications in electronics as magnetodielectrics, a surprisingly intense blue color was discovered when introducing Mn^{3+} into the trigonal bipyramidal (TBP) sites of hexagonal $YInO_3$.[15] This discovery startled the world, as brilliant blue oxides are rare and blue pigments based on Mn^{3+} as a chromophore were not known. Both end members, $YInO_3$ and $YMnO_3$, can crystallize in an acentric hexagonal structure ($P6_3cm$) consisting of alternating layers of edge-shared YO_6 octahedra and corner-shared MO_5 (M = In, Mn) trigonal bipyramids (Figure 1).[16,17]

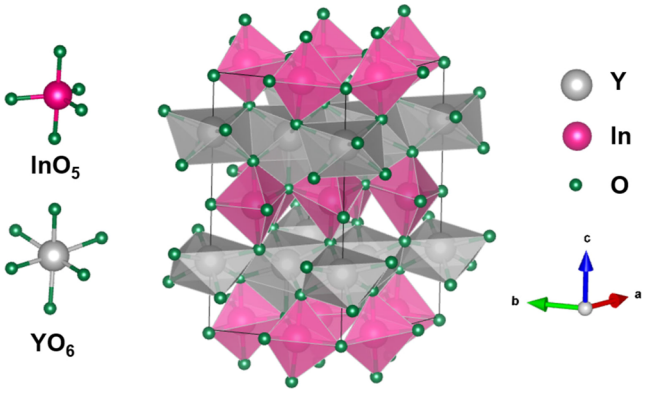

Figure 1. Schematic of the unit cell of $YInO_3$. YO_6 and InO_5 are shown by gray and magenta polyhedral, respectively.

The discovery of this intense blue color through Mn^{3+} substitution in TBP coordination inspired further exploration of related systems to identify other inorganic pigments with chromophore ions at TBP sites. Subsequent studies investigated the incorporation of various transition-metal ions, including Fe^{3+}, Cu^{2+}/Ti^{4+}, and $Mn^{3+}/Zn^{2+}/Ti^{4+}$, into the TBP positions of $YInO_3$.[18−20] Although $YIn_{1-x}(Co^{2+}_{0.5}Ti_{0.5})_xO_3$ and $YIn_{1-2x}Ti_x(Co^{2+}_{0.5}Zn_{0.5})_xO_3$ compositions were mentioned in a previous review article, a comprehensive synthesis, structural, magnetic, and optical analysis of these systems has not yet been reported.[20,21]

In the present work, we have investigated solid solutions $YIn_{1-x}(Co^{2+}_{0.5}Ti_{0.5})_xO_3$ (x = 0−0.4) and $YIn_{1-2x}Ti_x(Co^{2+}_{0.5}Zn_{0.5})_xO_3$ (x = 0−0.25), $YIn_{1-x}(Mn_{0.5}Ti_{0.5})_xO_3$ (x = 0−0.5), $YIn_{1-x}(Ni_{0.5}Ti_{0.5})_xO_3$ (x = 0−0.3), and $YIn_{1-x}(Fe_{0.5}Ti_{0.5})_xO_3$ (x = 0−0.3) with hexagonal structures to develop intense pigments and to understand the role of oxidation state and coordination environment on the resulting color. Tunable magenta, olive green, lime green and brown colors were discovered in these compositions, respectively. All the solid solutions were synthesized under a vacuum atmosphere to ensure the +2 oxidation state of Co, Mn, Ni, and Fe chromophores. Upon reheating in air, all compositions except the Ni-containing series show noticeable color changes that are largely reversible upon subsequent reduction, with the colors returning close to the original shades. This reversible color behavior is associated with oxidation-state changes of the Mn, Co, and Fe transition-metal chromophores, whereas Ni remains in the divalent state.

EXPERIMENTAL SECTION

Polycrystalline samples of $YIn_{1-x}(M^{2+}_{0.5}Ti_{0.5})_xO_3$ (M = Co, Mn, Ni, Fe) and $YIn_{1-2x}Ti_x(Co^{2+}_{0.5}Zn_{0.5})_xO_3$ were prepared following the standard solid-state synthesis method. Typical syntheses were carried out on a 5 g scale for each composition by thoroughly mixing stoichiometric amounts of Y_2O_3 (Nucor Research chemical, 99.9%), In_2O_3 (CERAC, 99.99%), ZnO (Sigma-Aldrich, 99.99%), TiO_2 (Aldrich, 99.9%), and $MTiO_3$ (M = Co, Mn, Ni, Fe) using an agate mortar and pestle. The pelletized mixture was then sealed in a fused silica ampule under vacuum (10^{-4} mm Hg) to ensure the +2 oxidation state of Co, Mn, Ni, and Fe in the solid solutions. Sealed samples were heated between 1300 and 1350 °C for 1 h in an MTI furnace with heating and cooling rates of 10 °C/min and 20 °C/min, respectively. The samples were reground and reheated repeatedly to complete the reaction. Y_2O_3 was dried overnight at 850 °C to remove any moisture and CO_2. $MTiO_3$ (M = Co, Mn, Ni, Fe) was synthesized in the laboratory by mixing stoichiometric amounts of Co_3O_4 (Alfa Aesar, 99.99%), $MnCO_3$ (Alfa Aesar, 99.9%), NiO (Alfa Aesar, 99.99%), FeO (Alfa Aesar, 99.5%), and TiO_2 (Aldrich, 99.9%). The mixture was then pelletized and heated between 900 and 1000 °C in an MTI furnace for 12 h. $FeTiO_3$ was synthesized in sealed tubes to prevent the oxidation of Fe^{2+} to Fe^{3+} in air. For comparison, samples were also prepared by heating the pelletized mixtures at 1300 °C for 24 h in air with intermediate grinding, followed by reduction in a 5% H_2/95% N_2 atmosphere at 550 °C for 5 h. Phase purity and unit cell parameters were determined using powder X-ray diffraction (XRD) on a benchtop Rigaku Miniflex II powder diffractometer with Cu Kα radiation and a graphite monochromator on the diffracted beam. Silicon powder was used as an internal standard to ensure accurate determination of unit cell dimensions. Lattice parameters were refined by LeBail fit using GSAS EXPGUI.[22] Powder neutron diffraction data of selected samples were collected on the 32-counter high-resolution diffractometer BT-1 at the Center for Neutron Research at the National Institute of Standards and Technology. A Cu(311) monochromator, yielding a wavelength of 1.5403(2) Å, was employed. Collimation of 15′ of arc was used before the monochromator, 20′ before the sample, and 7′ before the detectors. The samples (≈10 g) were loaded into vanadium containers 15.6 mm in diameter and 50 mm in length. Data were collected at room temperature over a 2θ range of 3°−167°. Structural refinements of neutron data were performed using GSAS-EXPGUI software.[22] Bond-valence analysis made use of VESTA.[23] Magnetic measurements (2−350 K) of selected solid solutions were obtained using a Quantum Design MPMS.[24] Diffuse reflectance data (up to 2500 nm) were collected using a Jasco V-670 spectrophotometer and converted to absorbance using the Kubelka−Munk equation.[25] A Konica Minolta CM-700d spectrophotometer (standard illuminant D65) was used to measure the L^*, a^*, b^* color coordinates.[26] Selected samples were stirred in pH 1 HNO_3 (aq.) and pH 12 NaOH (aq.) for 4 h, dried, and their color properties and phase purity were evaluated using a colorimeter and XRD to assess acid and base resistance. X-ray absorption spectroscopy (XAS) data at the Co and Ti K- and L-edges were collected on selected Co-containing samples at beamlines 4-ID-D and 29-ID of the Advanced Photon Source at Argonne National Laboratory. The K-edge measurements were done on powder samples using partial fluorescence yield detection by discriminating Co Kα and Ti Kα emission with a 4-element silicon drift diode detector. The L-edge measurements were done in total electron yield mode (drain current) using powder samples pressed onto indium foil. All XAS measurements were done at room temperature.

RESULTS AND DISCUSSION

The substitution of divalent chromophores M^{2+} (M = Co, Co/Zn, Mn, Ni, Fe) was attempted at the In site in various

https://doi.org/10.1021/acs.chemmater.6c01433
Chem. Mater. XXXX, XXX, XXX−XXX

$YIn_{1-x}(M^{2+}_{0.5}Ti_{0.5})_xO_3$ hexagonal systems. The maximum miscibility limits were determined from powder X-ray diffraction data. Compositions were considered single phase when all reflections could be indexed to the parent structure, whereas the appearance of additional diffraction peaks associated with residual starting materials and/or secondary impurity phases was taken as evidence that the miscibility limit had been exceeded. The maximum miscibility limits of Co, Mn, Ni, and Fe in the $YIn_{1-x}(M^{2+}_{0.5}Ti_{0.5})_xO_3$ solid solutions were determined to be x = 0.4, 0.5, 0.3, and 0.3, respectively, while the Co/Zn containing system, described by the composition $YIn_{1-2x}Ti_x(Co^{2+}_{0.5}Zn_{0.5})_xO_3$, exhibits a miscibility limit up to x = 0.25. The X-ray diffraction patterns of selected samples from the $YIn_{1-x}(M^{2+}_{0.5}Ti_{0.5})_xO_3$ (M = Co, Co/Zn, Mn, Ni, Fe) series are shown in Figure 2.

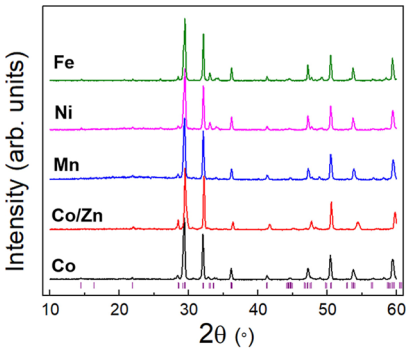

Figure 2. X-ray diffraction patterns of the $YIn_{0.8}(M^{2+}_{0.5}Ti_{0.5})_{0.2}O_3$ (M = Co, Mn, Ni, Fe) and $YIn_{0.6}Ti_{0.2}(Co^{2+}_{0.5}Zn^{2+}_{0.5})_{0.2}O_3$ compounds. The vertical bars (purple) indicate the expected reflection positions for the hexagonal ($P6_3cm$) phases.

The $YIn_{1-x}(Co^{2+}_{0.5}Ti_{0.5})_xO_3$ (x = 0−0.4) and $YIn_{1-2x}Ti_x(Co^{2+}_{0.5}Zn_{0.5})_xO_3$ (x = 0−0.25) solid solutions (made in a vacuum) exhibit tunable, intense magenta colors, with the zinc-containing samples appearing slightly lighter and brighter (Figure 3). The $YIn_{1-x}(Mn^{2+}_{0.5}Ti_{0.5})_xO_3$ (x = 0.0−0.5)

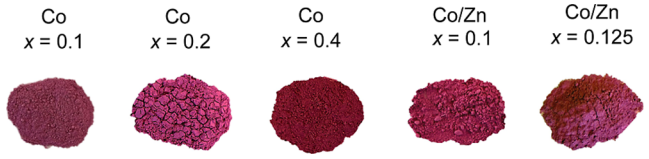

Figure 3. Images of selected $YIn_{1-x}(Co^{2+}_{0.5}Ti_{0.5})_xO_3$ (x = 0.1, 0.2, 0.4) and $YIn_{1-2x}Ti_x(Co^{2+}_{0.5}Zn_{0.5})_xO_3$ (x = 0.1, 0.125) compounds.

samples, show different shades of olive green. While the $YIn_{1-x}(Ni^{2+}_{0.5}Ti_{0.5})_xO_3$ (x = 0.0−0.3) series, show tunable lime green color, and the $YIn_{1-x}(Fe^{2+}_{0.5}Ti_{0.5})_xO_3$ (x = 0.0−0.3) samples differ in their brown coloration (Figure 4). The addition of M^{2+} (M = Co, Co/Zn, Mn, Ni, Fe) leads to unit cell shrinkage owing to the smaller size of M^{2+} (M = Co, Co/

Figure 4. Sample images of the $YIn_{0.8}(M^{2+}_{0.5}Ti_{0.5})_{0.2}O_3$ (M = Co, Mn, Ni, Fe) and $YIn_{0.6}Ti_{0.2}(Co^{2+}_{0.5}Zn^{2+}_{0.5})_{0.2}O_3$ compounds.

Zn, Mn, Ni, Fe) relative to In^{3+}.[27] Figure S1 shows the reduction of the lattice parameter resulting from M^{2+} substitution in $YIn_{1-x}(M^{2+}_{0.5}Ti_{0.5})_xO_3$ solid solutions, using M = Mn as an example.

Neutron powder diffraction data were collected and refined for two samples with intense magenta colors, $YIn_{0.6}Ti_{0.2}Co_{0.2}O_3$ and $YIn_{0.5}Ti_{0.25}Co_{0.125}Zn_{0.125}O_3$. The results of Rietveld refinement are shown in Figure 5, Tables 1, and S1. The χ^2 and wR_p for both Rietveld refinements are around 1.49 and 6.32%, respectively, indicating excellent agreement between the observed and calculated diffraction profiles. The occupancies of In, Co, and Ti were refined freely while constraining the total occupancy of the cation site to unity. The refined occupancies agree well with the nominal compositions, confirming the intended stoichiometry. Reliable occupancy refinement is possible because In, Co, and Ti exhibit significantly different coherent neutron scattering lengths (In = 4.065 fm, Co = 2.49 fm, and Ti = −3.438 fm). In particular, the negative scattering length of Ti provides strong contrast relative to In and Co, allowing the cation distributions to be determined with confidence.

The color of these materials has been evaluated using the CIE $L^*a^*b^*$ color space. It is a three-dimensional color model where $L^*a^*b^*$ uses three primary numbers to quantify the brightness (L^*), green−red (a^*), and blue−yellow (b^*) values (Figure S2). Higher L^* values are the result of brighter colors with a higher light reflectivity. Positive a^* values correspond to more red coloration, while more negative b* values are more blue. The $L^*a^*b^*$ color coordinates for selected samples from all $YIn_{1-x}(M^{2+}_{0.5}Ti_{0.5})_xO_3$ (M = Co, Co/Zn, Mn, Ni, Fe) series are mentioned in Table 2.

$YIn_{1-x}(M^{2+}_{0.5}Ti_{0.5})_xO_3$ (M = Co, Co/Zn) samples exhibited positive a^* (reddish hue) and negative b^* (bluish hue) values, consistent with their visually observed magenta shades. The $L^*a^*b^*$ data for samples from other series also show strong agreement with their visual appearance, further confirming the tunable optical properties achieved through compositional variation, as summarized in Table 2.

To evaluate the chemical stability of the pigments, acidic and basic stability tests were performed on selected samples from the $YIn_x(M^{2+}_{0.5}Ti_{0.5})_{1-x}O_3$ (M = Co, Co/Zn) series. The pigments were stirred in acidic (HNO_3, pH ≈ 1) and basic (NaOH, pH ≈ 12) solutions, and the treated samples were analyzed using CIE $L^*a^*b^*$ color space and X-ray diffraction (XRD). The total color difference (ΔE°), calculated as $\Delta E^\circ = \sqrt{(\Delta L^*)^2 + (\Delta a^*)^2 + (\Delta b^*)^2}$, serves as a quantitative measure of color change and thus reflects chemical stability after chemical exposure. For $YIn_{0.8}(Co_{0.5}Ti_{0.5})_{0.2}O_3$, the ΔE° values were 0.82 after HNO_3 treatment and 3.24 after NaOH treatment. For $YIn_{0.6}Ti_{0.2}(Co^{2+}_{0.5}Zn_{0.5})_{0.2}O_3$, the corresponding ΔE° values were 3.38 and 6.48, respectively. The ΔE° value below 1 observed for $YIn_{0.8}(Co_{0.5}Ti_{0.5})_{0.2}O_3$ after acid treatment indicates an essentially imperceptible color change, while the remaining values correspond to only slight to moderate color differences despite exposure to highly aggressive acidic (pH ≈ 1) and basic (pH ≈ 12) environments. Furthermore, XRD patterns remained unchanged after both acid and base treatments (Figure S3), indicating that the crystal structures were preserved.

The combination of low ΔE° values and unchanged XRD patterns demonstrates the excellent chemical stability of these pigments. Similar tests conducted on samples from other series

https://doi.org/10.1021/acs.chemmater.6c01433
Chem. Mater. XXXX, XXX, XXX−XXX

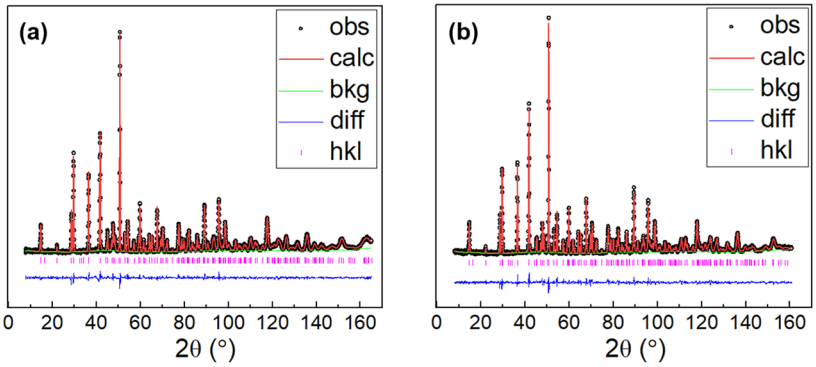

Figure 5. Rietveld refinement fits of neutron powder diffraction data for (a) $YIn_{0.6}Ti_{0.2}Co_{0.2}O_3$ and (b) $YIn_{0.5}Ti_{0.25}Co_{0.125}Zn_{0.125}O_3$, showing intense magenta color. Vertical bars (pink) denote the expected (*hkl*) Bragg reflection positions for the hexagonal ($P6_3cm$) phase.

Table 1. Neutron Refinement Result for $YIn_{0.6}Ti_{0.2}Co_{0.2}O_3$ Sample

atoms	Wyckoff position	*X*	*y*	*z*	occupancy	U_{iso} (Å^2)
Y1	2a	0.0	0.0	0.0557(6)	1.0	0.0117(21)
Y2	4b	0.3333	0.6667	0.0208(5)	1.0	0.0027(7)
In1	6c	0.3408(28)	0.0	0.7861(18)	0.623(4)	0.0054(12)
Co2	6c	0.3408(28)	0.0	0.7861(18)	0.203(4)	0.0054(12)
Ti	6c	0.3408(28)	0.0	0.7861(18)	0.174(4)	0.0054(12)
O1	6c	0.3092(8)	0.0	0.9587(7)	1.0	0.0061(16)
O2	6c	0.6399(8)	0.0	0.1225(7)	1.0	0.0072(17)
O3	2a	0.0	0.0	0.2550(9)	1.0	0.0111(20)
O4	4b	0.3333	0.6667	0.8059(6)	1.0	0.0222(11)

Table 2. *L*a*b Color Coordinates of $YIn_{1-x}(M^{2+}_{0.5}Ti_{0.5})_xO_3$ (M = Co, Co/Zn, Mn, Ni, Fe)**

composition	*L**	*a**	*b**
$YIn_{0.9}(Co_{0.5}Ti_{0.5})_{0.1}O_3$	44.81	16.38	−5.40
$YIn_{0.8}(Co_{0.5}Ti_{0.5})_{0.2}O_3$	42.19	19.9	−2.2
$YIn_{0.7}(Co_{0.5}Ti_{0.5})_{0.3}O_3$	36.9	22.96	−1.69
$YIn_{0.6}(Co_{0.5}Ti_{0.5})_{0.4}O_3$	34.28	20.21	−1.65
$YIn_{0.6}Ti_{0.2}(Co^{2+}_{0.5}Zn_{0.5})_{0.2}O_3$	44.22	24.25	−3.79
$YIn_{0.5}Ti_{0.25}(Co^{2+}_{0.5}Zn_{0.5})_{0.25}O_3$	33.45	21.17	−3.73
$YIn_{0.8}(Mn_{0.5}Ti_{0.5})_{0.2}O_3$	33.66	−2.06	4.86
$YIn_{0.8}(Ni_{0.5}Ti_{0.5})_{0.2}O_3$	60.2	−3.13	30.21
$YIn_{0.8}(Fe_{0.5}Ti_{0.5})_{0.2}O_3$	40.8	3.38	13.12
$YIn_{0.8}(Co_{0.5}Ti_{0.5})_{0.2}O_3$−$HNO_3$[a]	41.96	20.6	−1.85
$YIn_{0.8}(Co_{0.5}Ti_{0.5})_{0.2}O_3$−NaOH[a]	39.03	19.59	−1.58
$YIn_{0.6}Ti_{0.2}(Co^{2+}_{0.5}Zn_{0.5})_{0.2}O_3$−$HNO_3$[a]	41.57	26.26	−3.19
$YIn_{0.6}Ti_{0.2}(Co^{2+}_{0.5}Zn_{0.5})_{0.2}O_3$−NaOH[a]	37.91	25.55	−3.05

[a]Data collected after soaking in pH 1 HNO_3 and pH 12 NaOH.

yielded comparable results. These findings confirm that $YIn_{1-x}(M^{2+}_{0.5}Ti_{0.5})_xO_3$ (M = Co, Co/Zn, Mn, Ni, Fe) pigments are resistant to degradation under harsh acidic and basic environments, making them promising candidates for durable coating applications.

To investigate the origin of color in these solid solutions, UV−vis−NIR absorption spectra were collected for selected compositions from each series (Figure 6). Absorption in the low-wavelength region (200−400 nm) is attributed primarily to ligand-to-metal charge-transfer (LMCT) transitions, including $O^{2-} \rightarrow Ti^{4+}$ and $O^{2-} \rightarrow M^{2+}$ (M^{2+} = Co^{2+}, Mn^{2+}, Ni^{2+}, Fe^{2+}). The tailing of these intense charge-transfer bands into the visible region contributes significantly to the observed coloration.

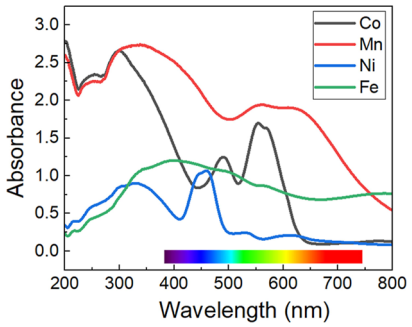

Figure 6. UV−vis absorbance spectra of $YIn_{1-x}(M^{2+}_{0.5}Ti_{0.5})_xO_3$ (M = Co, Mn, Ni, Fe).

In addition to these features, distinct absorption bands observed in the visible and near-infrared (NIR) regions originate from d−d transitions of M^{2+} ions (Co^{2+}: d^7, Mn^{2+}: d^5, Ni^{2+}: d^8, Fe^{2+}: d^6) in trigonal bipyramidal (TBP) coordination. A crystal-field splitting energy diagram for chromophores in an ideal TBP environment with D_{3h} symmetry is shown in Figure 7. Trigonal bipyramidal

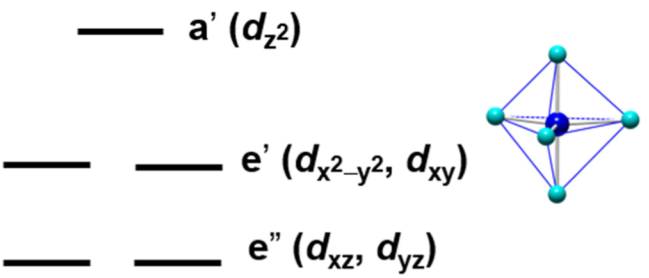

Figure 7. Ideal crystal field splitting energy diagram for TBP (D_{3h}).

https://doi.org/10.1021/acs.chemmater.6c01433
Chem. Mater. XXXX, XXX, XXX−XXX

coordination is relatively uncommon in extended oxide solids, and due to its lower symmetry, Tanabe−Sugano diagrams are not available. Consequently, the observed optical features are interpreted qualitatively using ideal TBP crystal-field splitting, with representative transitions such as $e'' \rightarrow a'$, $e' \rightarrow a'$, and available correlation diagrams developed for five-coordinate complexes (Figures 7 and 8).[15,28−30]

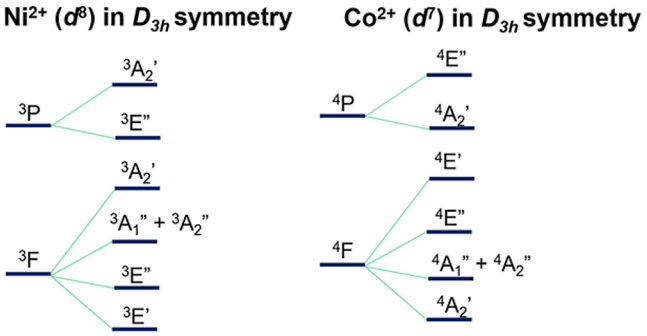

Figure 8. Correlation diagrams for Ni^{2+} (left) and Co^{2+} (right) with D_{3h} symmetry.

Correlation diagrams for trigonal bipyramidal (TBP) coordination are influenced by multiple parameters and not solely by crystal-field splitting. For Co^{2+} and Ni^{2+} in TBP coordination, available correlation diagrams that account for these parameters provide a framework for qualitative interpretation of the observed optical features. Based on structural refinement results and reasonable estimates of the relevant parameters, qualitative peak assignments using these correlation diagrams can be made for Ni^{2+} and Co^{2+}.

For Ni^{2+} (d^8), the absorption feature near ∼450 nm is assigned to overlapping $^3E'(^3F) \rightarrow {}^3A_2'$ and $^3E''(^3P)$ transitions. The band near ∼525 nm corresponds to the $^3E'(^3F) \rightarrow {}^3A_2'(^3P)$ transition, while the ∼600 nm feature is attributed to the $^3E'(^3F) \rightarrow {}^3A_1'' + {}^3A_2''(^3F)$ transitions. The NIR absorption near ∼1100 nm is assigned to the $^3E'(^3F) \rightarrow {}^3E''(^3F)$ transition, consistent with reported TBP-coordinated Ni^{2+} complexes (Figure 8).[29]

For Co^{2+} (d^7), the visible absorption near ∼500 nm is assigned to overlapping $^4A_2'(^4F) \rightarrow {}^4A_2'$ and $^4E''(^4P)$ transitions. The ∼550 nm band corresponds to the $^4A_2'(^4F) \rightarrow {}^4E'(^4F)$ transition, while the absorptions near ∼800 nm and ∼1200 nm are attributed to the $^4A_2'(^4F) \rightarrow {}^4E''(^4F)$ and $^4A_2'(^4F) \rightarrow {}^4A_1'' + {}^4A_2''(^4F)$ transitions, respectively (Figure 8).[28,29]

Precise assignment of individual absorption bands would require detailed theoretical calculations as well as single-crystal optical spectroscopy. Nevertheless, the UV−vis−NIR data indicate that the observed colors in these solid solutions arise from a combination of charge-transfer transitions and d−d transitions associated with TBP-coordinated M^{2+} ions.

In addition to color, we evaluated $YIn_{1-x}(M^{2+}_{0.5}Ti_{0.5})_xO_3$ samples for near-infrared (NIR) reflectivity, an important indicator of heat-reflective, energy-saving pigments.[31] As shown in Figure 9, Co-doped samples exhibit 50−80% NIR reflectance with a broad dip between 1000 and 1200 nm, while Ni-doped samples show 45−70% reflectance with a dip near 1200 nm. Mn and Fe doped samples show higher reflectivity, with Mn reaching 70−80% and Fe 60−70% across the 1200−2500 nm range. These high NIR reflectance values highlight

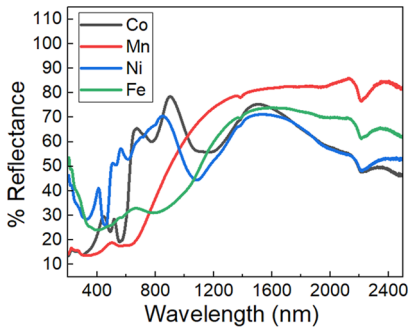

Figure 9. NIR reflectance of $YIn_{1-x}(M^{2+}_{0.5}Ti_{0.5})_xO_3$ (M = Co, Mn, Ni, Fe).

the potential of these materials for energy-efficient, NIR-reflective applications.

To confirm the oxidation states of the transition-metal ions in the synthesized $YIn_{1-x}(M^{2+}_{0.5}Ti_{0.5})_xO_3$ hexagonal systems, magnetic susceptibility measurements were performed on selected compositions. The temperature dependence of magnetic susceptibility (χ) is shown in Figure 10a. From the linear high-temperature region (150−350 K) of the inverse susceptibility ($1/\chi$) vs temperature plots (Figure 10b), Curie constants (C) were determined. The effective magnetic moment (μ_{eff}) was then calculated using the relation (eq 1)

$$\mu_{eff} = \sqrt{\frac{3k_B C}{N_A \mu_B^2}} \quad (1)$$

where k_B is the Boltzmann constant, C is the Curie constant, N_A is Avogadro's number, and μ_B is the Bohr magneton.

For the $YIn_{1-x}(Co^{2+}_{0.5}Ti_{0.5})_xO_3$ series, the inverse magnetic susceptibility ($1/\chi$) versus temperature (T) plots exhibit a downward curvature, indicating the presence of temperature-independent contributions, primarily arising from Van Vleck susceptibility (χ_{vv}). After subtracting χ_{vv}, the slope of the high-temperature linear region (150−300 K) of the $1/\chi$ versus T plots was used to determine the Curie constants (C). The resulting μ_{eff} values are higher than the spin-only moment expected for high-spin d^7 Co^{2+} in trigonal bipyramidal (TBP) coordination, consistent with previous reports of high-spin Co^{2+} complexes in TBP geometry, where enhanced magnetic moments arise from orbital contributions (Table 3).[29]

For the Mn, Ni, and Fe containing series, the inverse magnetic susceptibility ($1/\chi$) versus temperature (T) plots remain almost linear over the measured temperature range. For the Mn and Ni series, the experimentally determined μ_{eff} values closely match the expected spin-only magnetic moments. In contrast, the μ_{eff} values for the Fe series are higher than the spin-only values, owing to orbital contributions (Table 3).[32] Additional magnetic fitting parameters, including the Curie constants (C) and Curie−Weiss temperatures (θ_{CW}) obtained from Curie−Weiss fitting of the magnetic susceptibility data, are summarized in Table S2 of the Supporting Information.

Overall, the magnetic results confirm the +2 oxidation state of the doped transition metals in the $YIn_{1-x}(M^{2+}_{0.5}Ti_{0.5})_xO_3$ series.

After reheating the samples synthesized in sealed quartz tubes in air, all compositions exhibited a noticeable color change, except for the Ni-containing samples, which showed only subtle variations (Table S3) (Figure 11). Notably, samples synthesized directly in air exhibited the same color

https://doi.org/10.1021/acs.chemmater.6c01433
Chem. Mater. XXXX, XXX, XXX−XXX

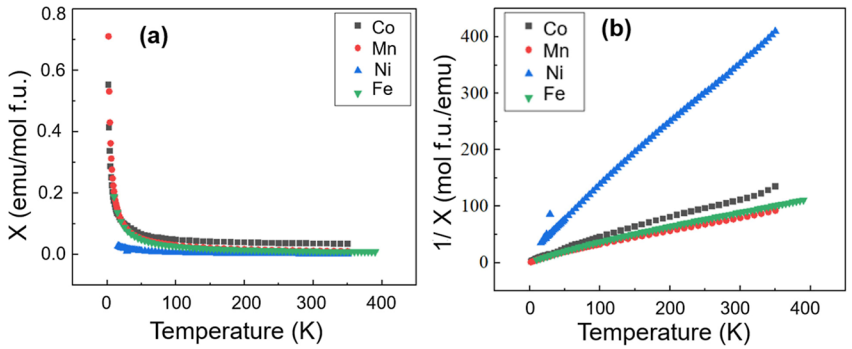

Figure 10. (a) Magnetic susceptibility and (b) inverse magnetic susceptibility of $YIn_{1-x}(M^{2+}_{0.5}Ti_{0.5})_xO_3$ (M = Co, Mn, Ni, Fe) as a function of temperature. One emu (cgs units) = 10^{-3} A m^2 (SI units).

Table 3. Calculated Spin-Only Magnetic Moment, Experimental Magnetic Moment, for $YIn_{1-x}(M^{2+}_{0.5}Ti_{0.5})_xO_3$ (M = Co, Mn, Ni, Fe)

composition	μ_S/B.M. (spin only)	μ_{exp}/B.M. (Experimental)
$YIn_{0.8}(Co_{0.5}Ti_{0.5})_{0.2}O_3$	3.87	4.15
$YIn_{0.8}(Mn_{0.5}Ti_{0.5})_{0.2}O_3$	5.92	5.89
$YIn_{0.8}(Ni_{0.5}Ti_{0.5})_{0.2}O_3$	2.83	2.77
$YIn_{0.8}(Fe_{0.5}Ti_{0.5})_{0.2}O_3$	4.90	5.64

Figure 11. Images of selected samples $YIn_{0.8}(M^{2+}_{0.5}Ti_{0.5})_{0.2}O_3$ (M = Co, Mn, Ni, Fe) after heating in sealed quartz tubes (top) and after heating in air (bottom). Samples are arranged from left to right.

as those obtained after reheating in air. Powder XRD patterns remained unchanged for both air-heated and sealed-tube samples, indicating that the long-range crystal structure was preserved (Figure S4). However, the observed color transformation suggests changes in oxidation state and/or subtle local structural distortions that are not detectable by powder XRD. Reheating the air-treated samples under reducing conditions resulted in a return to color shades similar to the original samples, confirming the reversibility of the process and suggesting that the color change originates primarily from oxidation of M^{2+} toward M^{3+}. In the Ni-containing samples, minor differences in hue may arise from variations in grain size or defect concentration.

To further understand the origin of these color changes, X-ray absorption spectroscopy (XAS), optical spectroscopy, and magnetic measurements were performed on selected air-heated samples and compared with those synthesized in sealed quartz tubes.

Three Co-containing samples were analyzed using XAS, two sealed quartz tube samples with intense magenta colors, $YIn_{0.6}Ti_{0.2}Co_{0.2}O_3$ and $YIn_{0.5}Ti_{0.25}Co_{0.125}Zn_{0.125}O_3$, and an air-made sample with a dark brown color, $YIn_{0.5}Ti_{0.25}Co_{0.125}Zn_{0.125}O_3$. The XAS spectra are shown in Figure 12a–d.

The Ti K-edge data for the 3 samples and the two references are shown in Figure 12a. The strong pre-edge peak displayed by the 3 samples indicates breaking of inversion symmetry at Ti sites, consistent with the trigonal bipyramidal environment (inversion symmetry is present at Ti sites in rutile TiO_2 and weakly broken in corundum Ti_2O_3). The energy of the pre-edge peak is known to be sensitive to coordination number, increasing by about 1 eV going from 4 to 6 coordination.[33] The main absorption edge (leading edge) of the three samples aligns very well with that of the TiO_2 reference, indicating that all 3 samples have Ti valence of 4+. Although the derivative shapes are complex (inset), the centroid of the leading edge derivative for all 3 samples and TiO_2 match quite well. There is no significant difference between sealed- and air-made samples (samples 2 and 3) indicating that Ti retains its 4+ oxidation state.

The Co K-edge data is shown in Figure 12b. The leading edge is broad, and the fine structure complex, a result of bandlike character of 4p states and related hybridization with 3d states especially in samples with tetrahedral sites (like Co_3O_4 and $CoAl_2O_4$). The pre-edge and leading edge in all three samples are proximate to those of the $CoAl_2O_4$ (Co^{2+}) reference sample. The two magenta samples (sealed tube, samples 1 and 2) have the same valence. The air-made, brown sample (sample 3) shows a small shift of pre-edge and leading edge to higher energies, indicating a higher charge state for Co ions, but significantly lower than 3+. This is consistent with the observation that the brown sample becomes dark magenta when reduced, presumably becoming closer to the vacuum-made samples with intense magenta colors.

The soft X-ray Ti and Co $L_{2,3}$ edge data are shown in Figure 12c,d. The "multiplet" fine structure arises from 2p to 3d (core–valence) and 3d–3d Coulomb and exchange interactions in the presence of the (spin–orbit–split) core state in the final, excited state of the X-ray absorption process. Together with crystal field and ligand charge-transfer excitations, this produces multiple discrete final state configurations.[34]

The Ti L-edge data for all 3 samples is indicative of a 4+ charge state, in agreement with conclusions from the Ti K-edge data. Note that the multiplet structure is influenced by the TBP crystal field acting on 3d states. Most significantly, there is no energy shifts or changes in multiplet structure between air and sealed samples indicating the magenta to brown color change between samples 2 and 3 is not associated with a change in oxidation state in Ti ions.

The Co L-edge (Figure 12d) data are indicative of a predominant Co^{2+} charge state in high-spin configuration, for all 3 samples. As with the Ti L-edge, the multiplet fine structure is influenced by the TBP coordination. There are no obvious changes in the energy position and fine structure

https://doi.org/10.1021/acs.chemmater.6c01433
Chem. Mater. XXXX, XXX, XXX–XXX

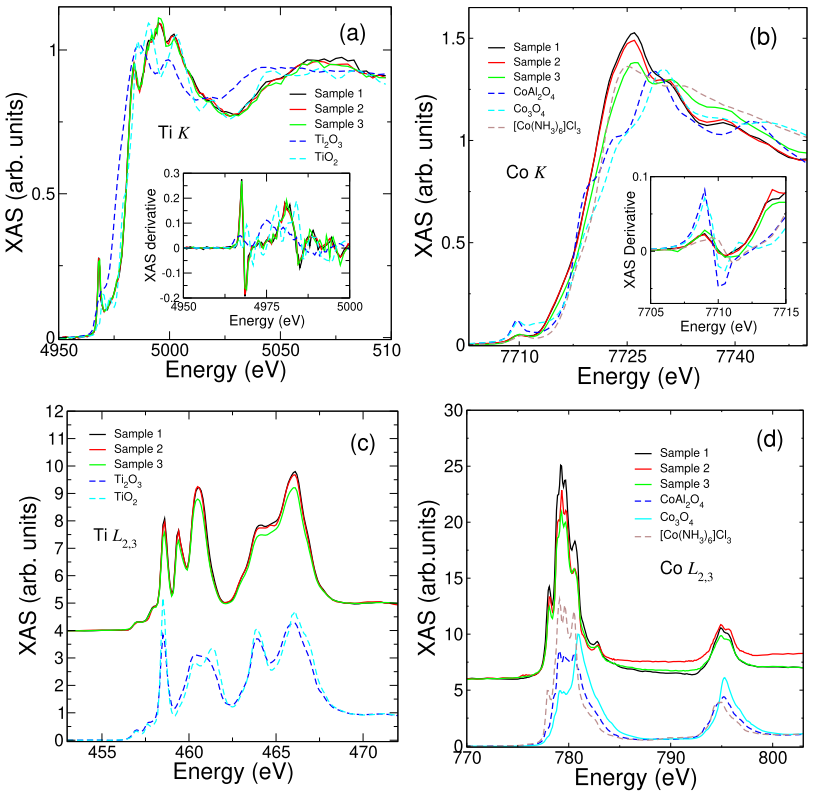

Figure 12. XAS spectra of selected Co-containing samples: sample 1 (magenta), vacuum-made $YIn_{0.6}Ti_{0.2}Co_{0.2}O_3$; sample 2 (magenta), vacuum-made $YIn_{0.5}Ti_{0.25}Co_{0.125}Zn_{0.125}O_3$; sample 3 (brown), air-made $YIn_{0.5}Ti_{0.25}Co_{0.125}Zn_{0.125}O_3$. From (a) to (d): (a) Ti K-edge, (b) Co K-edge, (c) Ti L-edge, (d) Co L-edge, insets in (a) and (b) are derivative plots.

between samples 2 and 3, indicating Co retains a predominant 2+ configuration. Unlike the Co K-edge data, where differences in oxidation state between samples 2 and 3 are apparent, the L-edge data does not capture this change. The K-edge is a bulk probe, while the L-edge total electron yield probe is strongly surface sensitive (1−3 nm typical). The combined K- and L-edge Co data point to the bulk of the sample dominating the optical absorption/scattering behind the color change, with the surface playing a less significant role.

Magnetic susceptibility measurements were performed on selected air-heated samples from each series. Magnetic susceptibilities were calculated per mole of magnetic ions, considering two possible oxidation-state scenarios: (i) M^{3+} + Ti^{3+} and (ii) M^{2+} + Ti^{4+}. In scenario (i), both M^{3+} and Ti^{3+} contribute to the total magnetic moment, whereas in scenario (ii) only M^{2+} is magnetic as Ti^{4+} is diamagnetic.

For the mixed-valence case (M^{3+} + Ti^{3+}), the expected effective magnetic moment was calculated using a mole-fraction-weighted expression (eq 2)

$$\mu_{\text{eff}} = \sqrt{x_{M^{3+}}(\mu_{M^{3+}})^2 + x_{\text{Ti}^{3+}}(\mu_{\text{Ti}^{3+}})^2} \quad (2)$$

where $x_{M^{3+}}$ and $x_{\text{Ti}^{3+}}$ are the mole fractions of M^{3+} and Ti^{3+}, respectively, and $\mu_{M^{3+}}$ and $\mu_{\text{Ti}^{3+}}$ are their corresponding spin-only magnetic moments. For the M^{2+} + Ti^{4+} scenario, the effective magnetic moment simplifies to (eq 3)

$$\mu_{\text{eff}} = \mu_{M^{2+}} \quad (3)$$

where $\mu_{M^{2+}}$ is the spin-only magnetic moment of M^{2+}.

Experimental effective magnetic moments were obtained from the linear high-temperature region (150−350 K) of inverse molar susceptibility ($1/\chi$) versus temperature plots by performing two separate Curie−Weiss fits of the experimental data, corresponding to the M^{3+}/Ti^{3+} and M^{2+}/Ti^{4+} oxidation-state scenarios. Curie constants (C) were extracted from these fits, and μ_{eff} values were calculated using eq 1. The experimentally derived magnetic moments from both fitting approaches were then compared with the theoretically calculated values for each scenario.

For the Mn-containing series, the experimentally observed magnetic moments agree well with the M^{3+}/Ti^{3+} model, supporting oxidation from Mn^{2+} to Mn^{3+} upon heating in air. In contrast, for the Fe and Co containing series, experimental magnetic moments extracted under both the M^{3+}/Ti^{3+} and M^{2+}/Ti^{4+} assumptions deviate from their respective spin-only theoretical values. As a result, magnetism alone does not allow a definitive distinction between the two oxidation-state scenarios, suggesting that one or both oxidation states may be present. For the Ni-containing series, the magnetic susceptibility closely matches the M^{2+}/Ti^{4+} scenario, indicating Ni remains in the +2 oxidation state after air heating.

In the $YIn_{1-x}(Mn_{0.5}Ti_{0.5})_xO_3$ samples, the sealed-tube and air-heated UV−vis spectra display similar peak positions. However, the air-heated samples show a clear increase in absorption intensity across both the UV and visible regions. In particular, the ratio of visible-region absorption to UV-region absorption increases after heating in air, supporting oxidation. This behavior is consistent with the expected optical differences between Mn^{2+}, which exhibits weak, spin-forbidden transitions, and Mn^{3+}, which shows stronger, spin-allowed transitions. The spectral shape and intensity of the air-heated samples also closely resemble those of $YInMnO_3$, further

https://doi.org/10.1021/acs.chemmater.6c01433
Chem. Mater. XXXX, XXX, XXX−XXX

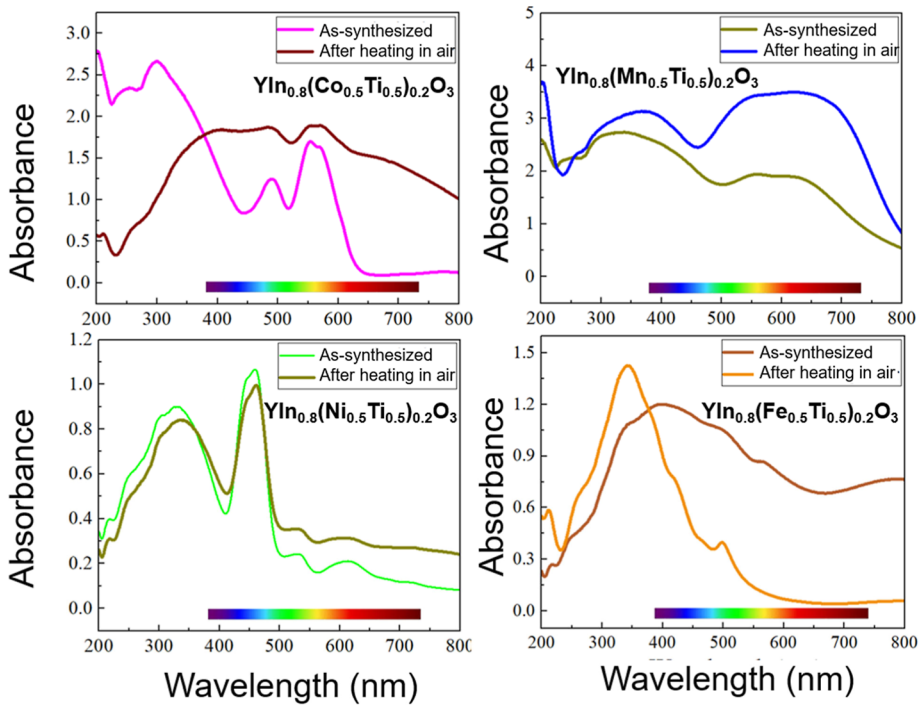

Figure 13. Comparison of UV−vis absorbance spectra of the $YIn_{0.8}(M^{2+}_{0.5}Ti_{0.5})_{0.2}O_3$ (M = Co, Mn, Ni, Fe) series before (as-synthesized) and after heating in air.

supporting oxidation from Mn^{2+} to Mn^{3+} and explaining the emergence of the characteristic blue color associated with Mn^{3+} in $YInMnO_3$ (Figure 13).[15]

In the $YIn_{1-x}(Ni_{0.5}Ti_{0.5})_xO_3$ system, the sealed-tube and air-heated spectra are nearly identical, with only minor differences in band intensity that follow the same overall trend. Combined with the magnetic analysis and the minimal color change observed upon air heating, these results indicate that Ni remains in the +2 oxidation state under air-heating conditions (Figure 13).

For $YIn_{1-x}(Co_{0.5}Ti_{0.5})_xO_3$, the optical spectra of air-heated samples show more pronounced differences relative to their sealed-tube counterparts. Changes in the UV region indicate differences in Co−O charge-transfer transitions associated with Co^{2+} versus Co^{3+}, while modifications in the visible region reflect changes in the electronic configuration that affect d−d transitions. Notably, spectral features characteristic of Co^{2+} remain present, indicating incomplete oxidation. These combined spectral changes, together with the observed color variation, support partial oxidation of Co^{2+} to Co^{3+} upon heating in air (Figure 13).

In the $YIn_{1-x}(Fe_{0.5}Ti_{0.5})_xO_3$ series, the air-heated samples exhibit noticeable differences in both the UV and visible regions compared with the sealed-tube samples. Changes in absorption intensity and spectral features suggest modifications in Fe−O charge-transfer transitions as well as Fe d−d transitions associated with Fe^{2+} and Fe^{3+}. The overall spectral appearance of the air-heated samples closely resembles that of Fe^{3+} in $YInFeO_3$ (Figure 13).[1]

The combined optical, magnetic, and X-ray absorption spectroscopy (XAS) analyses clearly demonstrate oxidation in the Mn, Co, and Fe-containing samples. In contrast, Ni shows minimal changes in optical absorption spectra and magnetic behavior, suggesting that Ni remains predominantly in the +2 oxidation state under both air-heated and sealed-tube conditions.

CONCLUSIONS

Polycrystalline samples of $YIn_{1-x}(M^{2+}_{0.5}Ti_{0.5})_xO_3$ (M = Co, Co/Zn, Mn, Ni, Fe) were successfully synthesized using a solid-state synthesis method and characterized structurally, optically, and magnetically. The maximum miscibility limits were determined to be x = 0.4 (Co), 0.5 (Mn), and 0.3 (Ni, Fe) in $YIn_{1-x}(M^{2+}_{0.5}Ti_{0.5})_xO_3$, while the Co/Zn-containing system ($YIn_{1-2x}Ti_x(Co^{2+}_{0.5}Zn_{0.5})_xO_3$) exhibits a limit of x = 0.25. The $YIn_{1-x}(Co^{2+}_{0.5}Ti_{0.5})_xO_3$ and $YIn_{1-2x}Ti_x(Co^{2+}_{0.5}Zn_{0.5})_xO_3$ solid solutions exhibited tunable intense magenta shades. The $YIn_{1-x}(Mn^{2+}_{0.5}Ti_{0.5})_xO_3$ series displayed olive-green hues, $YIn_{1-x}(Ni^{2+}_{0.5}Ti_{0.5})_xO_3$ showed tunable lime-green colors, and $YIn_{1-x}(Fe^{2+}_{0.5}Ti_{0.5})_xO_3$ exhibited varying brown shades. The origin of color in all solid solutions is attributed to combination of LMCT and d−d transitions. Optical and magnetic analyses confirmed the presence of the +2 oxidation state in the $YIn_{1-x}(M^{2+}_{0.5}Ti_{0.5})_xO_3$ (M = Co, Co/Zn, Mn, Ni, Fe) series. Among all compositions, the Co and Ni-based series exhibit intense magenta and lime-green colors, respectively. These pigments also demonstrated high near-infrared (NIR) reflectance and excellent chemical durability, making them promising candidates for energy-efficient coatings applications. Furthermore, their strong UV absorption enhances their functionality as protective colorants by reducing UV-induced polymer degradation in coating systems. Upon reheating in air, all compositions except the Ni-containing series show noticeable color changes that are largely reversible upon subsequent reduction, with colors returning to shades similar to the original samples. Combined optical, magnetic, and X-ray absorption spectroscopy analyses indicate oxidation of Mn, Co, and Fe from M^{2+} toward M^{3+}, whereas Ni remains in the +2 oxidation state. This behavior underscores the importance of

https://doi.org/10.1021/acs.chemmater.6c01433
Chem. Mater. XXXX, XXX, XXX−XXX

precise atmospheric control during synthesis to achieve the desired color. Overall, this study shows a rational way to design sustainable and intense inorganic pigments, where the coordination environment, oxidation state, and synthesis atmosphere together determine the final color and properties.

■ ASSOCIATED CONTENT

Supporting Information

The Supporting Information is available free of charge at https://pubs.acs.org/doi/10.1021/acs.chemmater.6c01433.

Unit-cell parameter trends for the Mn-containing solid-solution series; CIELAB color-space illustration; powder X-ray diffraction patterns before and after acid and base treatment; neutron powder diffraction refinement results; Curie−Weiss fitting parameters derived from magnetic susceptibility data; and *L*a*b** color coordinates for selected compositions before and after heating in air (PDF)

■ AUTHOR INFORMATION

Corresponding Author

M. A. Subramanian − *Department of Chemistry, Oregon State University, Corvallis, Oregon 97331, United States;* orcid.org/0000-0001-5487-043X; Email: mas.subramanian@oregonstate.edu

Authors

Anjali Verma − *Department of Chemistry, Oregon State University, Corvallis, Oregon 97331, United States*

Jun Li − *Department of Chemistry, Oregon State University, Corvallis, Oregon 97331, United States*

Chung Yi Hsu − *Department of Chemistry, Oregon State University, Corvallis, Oregon 97331, United States*

Arthur P. Ramirez − *Department of Physics, University of California, Santa Cruz, California 95064, United States*

Fanny Rodolakis − *Advanced Photon Source, Argonne National Laboratory, Lemont, Illinois 60439, United States*

Daniel Haskel − *Advanced Photon Source, Argonne National Laboratory, Lemont, Illinois 60439, United States;* orcid.org/0000-0002-5532-5908

Complete contact information is available at: https://pubs.acs.org/10.1021/acs.chemmater.6c01433

Author Contributions

Anjali Verma: Conceptualization, Formal analysis, Methodology, Investigation, Writing—original draft, Writing—review and editing. **Jun Li:** Writing—review and editing, Investigation, Formal analysis, Validation. **Chung Yi Hsu:** Investigation, Formal analysis, Validation. **Arthur P. Ramirez:** Writing—review and editing, Validation, Investigation, Formal analysis. **Fanny Rodolakis:** Investigation, Formal analysis, Validation. **Daniel Haskel:** Writing—review and editing, Validation, Investigation, Formal analysis. **M. A. Subramanian:** Supervision, Project administration, Investigation, Funding acquisition, Formal analysis, Conceptualization, Writing—review and editing.

Notes

The authors declare no competing financial interest.

■ ACKNOWLEDGMENTS

The work done at Oregon State University was supported by NSF Grant No. DMR-2025615 (M.A.S.). The work done at UC, Santa Cruz (A.P.R.) was supported by NSF Grant No. DMR-2218130. The work at the Advanced Photon Source of Argonne National Laboratory was supported by the U.S. DOE Office of Science, Office of Basic Energy Sciences, under Contract No. DE-AC0206CH11357.

■ REFERENCES

(1) Subramanian, M. A.; Li, J. YInMn Blue - 200 Years in the Making: New Intense Inorganic Pigments Based on Chromophores in Trigonal Bipyramidal Coordination. *Mater. Today Adv.* **2022**, *16*, 100323.

(2) Buxbaum, G.; Pfaff, G. *Industrial Inorganic Pigments, Completely Revised and Extended*, 3rd ed.; Wiley-VCH: Weinheim, 2005.

(3) *High Performance Pigments*; Smith, H. M., Ed.; Wiley-VCH: Weinheim, 2002.

(4) Jeevanandam, P.; Mulukutla, R. S.; Phillips, M.; Chaudhuri, S.; Erickson, L. E.; Klabunde, K. J. Near Infrared Reflectance Properties of Metal Oxide Nanoparticles. *J. Phys. Chem. C* **2007**, *111* (5), 1912−1918.

(5) Huang, Y.-A.; Li, J.; Ramirez, A. P.; Subramanian, M. A. New Solid Solutions with the R-Type Hexaferrite Structure, $Ba-Fe_{4-x}M_xM'_2O_{11}$ (M = In, Sc; M' = Ti, Sn). *Prog. Solid State Chem.* **2024**, *76*, 100494.

(6) Wang, Q.; Wang, Z.; Qi, M.; Zhao, H.; Xin, X.; Verma, A.; Siritanon, T.; Ramirez, A. P.; Subramanian, M. A.; Jiang, P. Synthesis and Optical Properties Based on Ni-Doped Zn_2SiO_4 Blue Pigments with High-NIR Reflectance. *ACS Sustain. Chem. Eng.* **2024**, *12* (14), 5522−5532.

(7) Lewis, P. A. C. Organic and Inorganic Pigments. In *Azimuth*; Elsevier, 1998; Vol. *1*, pp 283−312.

(8) Rao, C. N. R. Novel Materials, Materials Design and Synthetic Strategies: Recent Advances and New Directions. *J. Mater. Chem.* **1999**, *9* (1), 1−14.

(9) Nassau, K. The Origins of Color in Minerals. *Am. Mineral.* **1978**, *63* (3−4), 219−229.

(10) Nassau, K. The Fifteen Causes of Color. In *Azimuth*; Elsevier, 1998; Vol. *1*, pp 123−168.

(11) Subramanian, M. A.; Li, J. Challenges in the Rational Design of Intense Inorganic Pigments with Desired Colors. *Nat. Rev. Mater.* **2023**, *8* (2), 71−73.

(12) Albright, T. A.; Burdett, J. K.; Whangbo, M.-H. *Orbital Interactions in Chemistry*, 2nd ed.; Wiley-VCH: Weinheim, 2013.

(13) Verma, A.; Li, J.; Ramirez, A. P.; Subramanian, M. A. Understanding Color Variation with Site Distribution in Inverse Spinel Structure via Neutron Diffraction, Magnetism, and Optical Studies. *Prog. Solid State Chem.* **2024**, *74*, 100455.

(14) Verma, A.; Li, J.; Subramanian, M. A. Cr^{2+} in Square Planar Coordination: Durable and Intense Magenta Pigments Inspired by Lunar Mineralogy. *Chem. Mater.* **2024**, *36* (8), 3837−3843.

(15) Smith, A. E.; Mizoguchi, H.; Delaney, K.; Spaldin, N. A.; Sleight, A. W.; Subramanian, M. A. Mn^{3+} in Trigonal Bipyramidal Coordination: A New Blue Chromophore. *J. Am. Chem. Soc.* **2009**, *131* (47), 17084−17086.

(16) Pistorius, C. W. F. T.; Kruger, G. J. Stability and Structure of Noncentrosymmetric Hexagonal $LnInO_3$ (Ln = Eu, Gd, Tb, Dy, Ho, Y). *J. Inorg. Nucl. Chem.* **1976**, *38* (8), 1471−1475.

(17) Aken, B. B. V.; Meetsma, A.; Palstra, T. T. M. Hexagonal $YMnO_3$. *Acta Crystallogr. C* **2001**, *57* (3), 230−232.

(18) Smith, A. E.; Comstock, M. C.; Subramanian, M. A. Spectral Properties of the UV Absorbing and Near-IR Reflecting Blue Pigment, $YIn_{1-x}Mn_xO_3$. *Dyes Pigments* **2016**, *133*, 214−221.

(19) Li, J.; Lorger, S.; Stalick, J. K.; Sleight, A. W.; Subramanian, M. A. From Serendipity to Rational Design: Tuning the Blue Trigonal Bipyramidal Mn^{3+} Chromophore to Violet and Purple through

Application of Chemical Pressure. *Inorg. Chem.* **2016**, *55* (19), 9798−9804.
(20) Li, J.; Subramanian, M. A. Inorganic Pigments with Transition Metal Chromophores at Trigonal Bipyramidal Coordination: Y-(In,Mn)O_3 Blues and Beyond. *J. Solid State Chem.* **2019**, *272*, 9−20.
(21) Comstock, M. C.; Smith, A. E. Red and Red-Shade Violet Inorganic Oxide Materials Containing Cobalt. WO 2017070438 A1, 2017.
(22) Larson, A. C.; Dreele, R. B.; Toby, B. *General Structure Analysis System*; GSAS/EXPGUI, 1994; p 748.
(23) Momma, K.; Izumi, F. VESTA 3 for Three-Dimensional Visualization of Crystal, Volumetric and Morphology Data. *J. Appl. Crystallogr.* **2011**, *44* (6), 1272−1276.
(24) Lewis, L. H.; Bussmann, K. M. A Sample Holder Design and Calibration Technique for the Quantum Design Magnetic Properties Measurement System Superconducting Quantum Interference Device Magnetometer. *Rev. Sci. Instrum.* **1996**, *67* (10), 3537−3542.
(25) El Sherif, M.; Bayoumi, O. A.; Sokkar, T. Z. N. Prediction of Absorbance from Reflectance for an Absorbing-Scattering Fabric. *Color Res. Appl.* **1997**, *22* (1), 32−39.
(26) Minolta, I. K. Precise Color Communication; Konica Minolta, Inc., 2011. https://www.konicaminolta.com/instruments/knowledge/color/part1/07.html.
(27) Shannon, R. D. Revised Effective Ionic Radii and Systematic Studies of Interatomic Distances in Halides and Chalcogenides. *Acta Crystallogr., Sect. A:* **1976**, *32* (5), 751−767.
(28) Hunault, M.; Robert, J.-L.; Newville, M.; Galoisy, L.; Calas, G. Spectroscopic Properties of Five-Coordinated Co^{2+} in Phosphates. *Spectrochim. Acta, Part A Mol. Biomol. Spectrosc.* **2014**, *117*, 406−412.
(29) Morassi, R.; Bertini, I.; Sacconi, L. Five-Coordination in Iron(II); Cobalt(II) and Nickel(II) Complexes. *Coord. Chem. Rev.* **1973**, *11* (4), 343−402.
(30) Lin, Y.-C.; Verma, A.; Li, J.; Ramirez, A. P.; Subramanian, M. A. Intense Yellow/Orange/Red Pigments Based on a Thortveitite-like Structure without Toxic Elements: $Zn_{2-x}Ni_xV_2O_7$. *Chem. Mater.* **2025**, *37* (13), 4665−4673.
(31) Jose, S.; Joshy, D.; Narendranath, S. B.; Periyat, P. Recent Advances in Infrared Reflective Inorganic Pigments. *Sol. Energy Mater. Sol. Cells* **2019**, *194*, 7−27.
(32) Leclercq, B.; Kabbour, H.; Arevalo-Lopez, A.; Huvé, M.; Daviero-Minaud, S.; Minaud, C.; Blazquez Alcover, I.; Mentré, O. P. Phase Transitions and Stability in $BaM_2(PO_4)_2$ M = Mn, Fe, Co Systems. *Inorg. Chem. Front.* **2020**, *7* (1), 239−246.
(33) Henderson, G. S.; De Groot, F. M. F.; Moulton, B. J. A. X-Ray Absorption Near-Edge Structure (XANES) Spectroscopy. *Rev. Mineral. Geochem.* **2014**, *78* (1), 75−138.
(34) De Groot, F. M. F. X-Ray Absorption and Dichroism of Transition Metals and Their Compounds. *J. Electron Spectrosc. Relat. Phenom.* **1994**, *67* (4), 529−622.

https://doi.org/10.1021/acs.chemmater.6c01433
Chem. Mater. XXXX, XXX, XXX−XXX